THE JOURNAL OF PHYSICAL CHEMISTRY C

Article

Cite This: J. Phys. Chem. C 2019, 123, 20594−20604

pubs.acs.org/JPCC

Is There a Negative Thermal Expansion in Supported Metal Nanoparticles? An in Situ X-ray Absorption Study Coupled with Neural Network Analysis

Janis Timoshenko,[†] Mahdi Ahmadi,[‡] and Beatriz Roldan Cuenya*,[†,‡]

[†]Department of Interface Science, Fritz-Haber-Institute of the Max Planck Society, 14195 Berlin, Germany
[‡]Department of Physics, University of Central Florida, Orlando, Florida 32816, United States

Supporting Information

ABSTRACT: Interactions with their support, adsorbates, and unique structural motifs are responsible for many intriguing properties and potential applications of supported metal nanoparticles (NPs). At the same time, they complicate the interpretation of experimental data. In fact, the methods and approaches that work well for the ex situ analysis of bulk materials may be inaccurate or introduce artifacts in the in situ analysis of nanomaterials. Here, we revisit the controversial topic of negative thermal expansion and anomalies in the Debye temperature reported for oxide-supported metal NPs. In situ X-ray absorption experimental data collected for Pt NPs in ultrahigh vacuum and an advanced data analysis approach based on an artificial neural network demonstrate that Pt NPs do not exhibit intrinsic negative thermal expansion. Similarly, as for bulk materials, in the absence of adsorbates and strong particle-support interaction, the bond lengths in metal NPs increase with temperature. The previously reported anomalies in particle-size-dependent Debye temperatures can also be linked to the artifacts in the interpretation of conventional X-ray absorption data of disordered materials such as NPs.

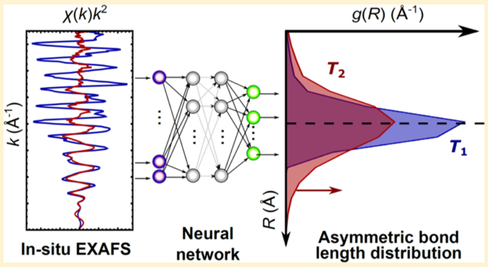

Metal nanoparticles (NPs) exhibit a large variety of intriguing structural and thermodynamic properties that differ from those of the corresponding bulk materials and that can have important implications for technological applications. These properties stem from the presence of unique structural motifs (e.g., undercoordinated surface sites), finite-size effects on their electronic structure,[1,2] and strong interactions between the NP support, ligands, and adsorbates.[3] For example, well known is the shortening of the interatomic distances with decreasing NP size associated with the minimization of the NP surface energy and the structure relaxation in near-surface layers.[4−7] Other properties of NPs, such as the melting temperature and related Debye temperature, are also known to be particle-size-dependent. Normally, for freestanding NPs, the reduction of the Debye and melting temperatures is expected due to surface-induced softening of the NP structure.[8−13] Nevertheless, examples of an opposite trend can also be found in the literature,[14−18] and in some cases, even a nonmonotonic relation between the NP size and the Debye temperature has been reported.[19] Such a nontrivial relationship between the thermal properties of a NP and its size has been attributed to the interplay between intrinsic NP characteristics and the details of the NP interactions with their environment (support and adsorbates). Intriguing and similarly controversial is also the topic of thermal expansion for nanoscale materials. Theory predicts that the thermal expansion coefficient in metallic NPs should be larger than that in the bulk material[19−23] due to excess volume available for atoms at the NP surface and reduced cohesive energy in smaller NPs. Much experimental evidence confirms this prediction.[9,10,24] At the same time, several studies have shown that, for some supported nanostructured metals metals, the thermal expansion coefficient is lower than that in bulk materials[25−27] or, as in the case of oxide-supported Pt NPs, even negative.[14,15,17,19]

The observation of negative thermal expansion (NTE) in Pt NPs is surprising since this effect is usually associated with open, framework-type materials that can be described as networks of rigid polyhedral units with low-frequency phonon modes,[28−34] materials where the valence state of lattice-forming atoms can change[33,35] or materials with magnetic interactions (Invar effect).[36−38] For close-packed nonmagnetic metals, NTE is not expected, except at very low temperatures, where electronic contributions to thermal expansion start to be important.[37,38] In nanoparticles, NTE has been observed in CuO and MnF_2 NPs and associated with magnetic interactions[39] and also in Au NPs where a crossover from positive to negative thermal expansion at about 125 K was ascribed to electronic excitations and their effect on the equilibrium interatomic distance.[25,26]

Previous works suggest that NTE in Pt NPs depends strongly on the particle size and is not observed for particles larger than 1−2 nm.[14,15,17,19] It is also a support-dependent

Received: May 28, 2019
Revised: July 16, 2019
Published: July 19, 2019

ACS Publications

DOI: 10.1021/acs.jpcc.9b05037
J. Phys. Chem. C 2019, 123, 20594−20604

effect: NTE was reported for Pt NPs on γ-Al_2O_3[14,15,17,19] but not for similar Pt NPs on carbon.[14,15] For the latter, the thermal expansion coefficient was found to be comparable to that of bulk Pt[14,15] or even larger than that.[21] Based on ab initio molecular dynamics (MD) simulations,[40] it was suggested that the observed NTE and enhanced Debye temperatures in this system are a result of dynamic particle—support interactions where temperature-dependent formation and breaking of Pt—O bonds with the support and charge transfer from the support result in a temperature-dependent effective Pt—Pt interatomic potential, which becomes deeper at higher temperatures.[14,40]

On the other hand, it was also proposed elsewhere[19] that the observed shortening of the Pt—Pt distance may not be an intrinsic property of Pt NPs but a result of temperature-dependent hydrogen coverage. Note that, to avoid the oxidation of the NPs, the majority of the temperature-dependent investigations so far have been carried out in a reducing hydrogen-rich atmosphere. It is known that the presence of hydrogen affects significantly the local structure around Pt atoms, reducing the disorder and increasing the Pt—Pt bond length.[14,15,17,19,41] Hydrogen coverage is strongly temperature-dependent, and hydrogen was reported to desorb completely at temperatures above 550 K.[41] Since the presence of hydrogen increases the bond length, hydrogen desorption with increasing sample temperature will result in reduced Pt—Pt distances, which may then be incorrectly attributed to an intrinsic NTE effect. According to Roldan Cuenya et al.,[19] the plausibility of this scenario was demonstrated based on ab initio MD simulations of Pt NPs with different numbers of adsorbed hydrogen atoms. This argument does not explain, however, why the NTE was observed (and even enhanced) also in reduced Pt NPs when measured in helium.[14,15,17] In these cases, particle-support interactions are believed to play a crucial role.[14,15]

Finally, note that the vast majority of the studies reporting NTE (and also enhanced Debye temperatures) in metal NPs were based on in situ extended X-ray absorption fine structure (EXAFS) measurements. This is due to the fact that NTE is not observed for large NPs and that X-ray diffraction (XRD) methods, commonly used to study NTE in bulk materials, are not applicable for the investigation of NPs with sizes smaller than a few nanometers. EXAFS spectroscopy, in turn, is a premier method for quantitative studies of NPs with sizes in the range of a few nanometers or smaller due to its high sensitivity to interatomic distances and the details of the local environment around the absorbing atoms[42] and its applicability to studies of a broad range of samples under a wide range of experimental conditions.[43−45] The sensitivity of the EXAFS method to thermal expansion of well-defined bulk materials has been demonstrated.[46−48] At the same time, it was also shown that, for nanomaterials, which have a significantly larger disorder than the corresponding bulk materials, the interpretation of the EXAFS results should be done with caution. It was demonstrated that, in the case of broad, non-Gaussian distributions of bond lengths, the conventional EXAFS fitting may result in inaccurate (typically underestimated) metal—metal distances, coordination numbers, and disorder factors.[49−57] This fact is especially important for small NPs[51,58] due to their enhanced structural disorder and for the analysis of EXAFS data collected at high temperatures. Neglecting or improper treatment of these non-Gaussian effects in NP bond length distributions thus can also be mistaken for an NTE effect, and, similarly, may result in overestimated values of the Debye temperatures.

The present study attempts to provide insight concerning the presence or the lack of anomalies in the thermal expansion and Debye temperatures of supported Pt NPs. First, on the experimental side, we carried out an in situ X-ray absorption spectroscopy (XAS) experiment for supported Pt NPs in ultrahigh vacuum (UHV) to avoid all NP/adsorbate interactions. Size-selected Pt NPs were prepared via the inverse micelle encapsulation method[59,60] and were deposited on single-crystal SiO_2/Si(111) supports. The EXAFS measurements were complemented with AFM and STM characterization to ensure narrow NP size and shape distributions, which is crucial for the interpretation of the results extracted from ensemble-averaging techniques such as EXAFS.

On the data analysis side of the problem, we employ here a recently developed advanced tool for the interpretation of XAS spectra in small metallic NPs: neural network (NN)-based analysis of EXAFS data.[61,62] In this approach, a large set of theoretically generated (using MD simulations) structures and the corresponding ab initio calculated[63] EXAFS spectra are used to train an NN, which is a composite function that assigns features of the EXAFS signal to the structural characteristics of the material. After the NN training is completed and the relation between spectral features and structure parameters is established, the NN can take as input experimental EXAFS data and yield as output the entire radial distribution function (RDF). As recently demonstrated,[61,62] this approach allows reliable reconstruction of the local environment characteristics both in bulk and disordered nanostructured materials, allowing us to probe directly the non-Gaussian shapes of RDF peaks to get access to the contributions of distant coordination shells (which are more sensitive to the thermal expansion) and to follow in situ their evolution.

By combining a state-of-the-art experiment design with an advanced approach for data analysis, we demonstrate in this study the subtleties of the interpretation of the NTE effect in nanoparticles. First, we show that, in the absence of hydrogen adsorbates, no bond length shortening can be observed in our data on preformed NPs (with low NP-support interaction) when the contribution of non-Gaussian effects is properly taken into account. For samples studied in a hydrogen atmosphere, in turn, the reduced or even slightly negative thermal expansion can be observed, but this shortening of bond distances is a local effect, linked to the changes in the shapes of the distributions of bond lengths between nearest neighbors, rather than to actual changes in the fcc lattice spacing. Thus, the previously reported NTE effect in Pt NPs is not the same as an intrinsic NTE observed in bulk materials. Similarly, we demonstrate also that the enhanced Debye temperatures, reported previously for small Pt NPs, are also an artifact of conventional EXAFS analysis. Our results, obtained via an NN-EXAFS analysis approach, show that the Debye temperature is the same as that in bulk materials for particles larger than 1 nm and is only significantly reduced for the NPs of sub-nanometer size, in agreement with the predictions from theoretical models.

■ EXPERIMENTS

Size-selected Pt NPs were synthesized using the inverse micelle encapsulation method. A commercial diblock copolymer poly(styrene)-*block*-poly(2-vinylpyridine) [PS(26000)-P2VP(4800)] was dissolved in toluene to form micelles.

Subsequently, $H_2PtCl_6{\cdot}6H_2O$ with a metal/P2VP ratio of 0.18 was added to the solution to create the metal NPs. A monolayer-thick film of NPs was obtained after dip-coating the natively oxidized SiO_2/Si(111) substrate into the micellar solution. An in situ O_2-plasma treatment at 5×10^{-6} mbar for 100 min was performed to remove the polymer. Morphology and size distributions of the synthesized NPs were controlled using a Veeco multimode AFM microscope (Nanoscope IIIa), as well as an STM (Aarhus STM, SPECS GmbH). In order to confirm the complete removal of the ligands, X-ray photoelectron spectroscopy (XPS) measurements were conducted using a monochromatic Al Kα X-ray source (1486.6 eV) and a Phoibos (SPECS) electron energy analyzer.[64]

XAS measurements were performed at the 12-BM beamline of the Argonne National Laboratory, which is equipped with a UHV chamber. The experiments were conducted in fluorescence mode at the Pt L_3-edge (11.6 keV). The samples were first transferred into the UHV chamber and annealed in O_2 at 723 K for 30 min for the removal of adventitious carbon species from the air sample transfer. Subsequently, the samples were reduced in vacuum at 873 K. XAFS measurements were then performed between room temperature and 723 K.

Reference XAFS data for Pt NPs on Al_2O_3[17] were collected at the X18B beamline of the NSLS I Facility at Brookhaven National Laboratory.

DATA ANALYSIS AND RESULTS

EXAFS Data and Conventional Analysis. Temperature-dependent experimental Pt L_3-edge XANES and EXAFS spectra acquired in UHV for Pt NPs deposited on single-crystal SiO_2/Si(111) are shown in Figure 1. Preliminary analysis of room temperature XAS data for this sample is presented elsewhere.[64] Narrow particle size distributions in this sample are confirmed by AFM (see Figure S1). The average particle height obtained by AFM was 1.8 ± 0.8 nm.

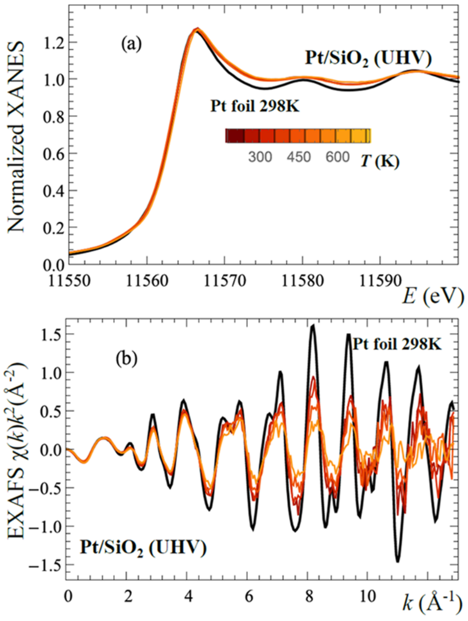

Figure 1. Experimental Pt L_3-edge XANES (a) and EXAFS (b) spectra for Pt NPs on SiO_2/Si(111) in UHV. Spectra for a Pt foil are also shown for comparison.

In addition to the interpretation of new Pt NP/SiO_2 data acquired in UHV, here, we also revisit the analysis of the EXAFS spectra of two samples (samples S2 and S3) from ref 17. These samples were prepared using an identical micelle encapsulation method but were deposited on γ-Al_2O_3. Average particle sizes, as established by TEM analysis, were 1.0 ± 0.2 nm for sample S2 and 0.8 ± 0.2 nm for sample S3. Particles of such sizes and on this support have been previously used in negative thermal expansion studies.[14,15,17,19] It should be noted, however, that the differences in NP shapes and internal order of samples prepared via different methods cannot be neglected, since strong NP-support interactions resulting in flat NP shapes are expected to play a role in the NTE. EXAFS data for these samples are shown in Figure S2. One should note that the better signal-to-noise ratio observed in these EXAFS data in comparison with that of our new Pt NP/SiO_2 sample is due to the fact that, in the latter case, a sub-monolayer NP coverage on a SiO_2/Si(111) single-crystal support was considered to ensure a very well defined sample structure. Nevertheless, this also resulted in a significantly lower metal loading in this sample as compared to the nanocrystalline powder-supported S2 and S3 Pt NP samples (and related samples previously described in the literature). Conventional EXAFS analysis, presented for S2 and S3 samples in ref 17, showed anomalous thermal properties for these samples: S3 exhibited NTE in a H_2 atmosphere, which was further found to be enhanced when measured under a He atmosphere. Sample S2 in hydrogen exhibited positive thermal expansion although lower than that in bulk Pt. At the same time, an anomalously large Debye temperature was observed for sample S2.

Note here that, in the conventional approach, the EXAFS spectrum $\chi(k)$ is commonly expressed as a sum of partial contributions from different scattering paths: $\chi(k) = \sum_p \chi_p(k)$, where the summation includes the contributions of single-scattering (SS) as well as multiple-scattering (MS) paths. Here, k is the photoelectron wavenumber with the equation

$$k = \sqrt{\frac{2m_e}{\hbar^2}(E - E_0)} \tag{1}$$

where m_e is the electron mass, $\hbar$ is Planck's constant, E is the X-ray photon energy, and E_0 is the photoelectron reference energy. For SS paths, one can write the relation between $\chi_p(k)$ and the corresponding bond length distribution $g_p(R)$ as[65,66]

$$\chi_p(k) = S_0^{\,2} \int_0^{+\infty} A_p(k, R) g_p(R) \sin(2kR + \varphi_p(k, R)) \frac{dR}{R^2} \tag{2}$$

Here, A_p and φ_p are the scattering amplitude and phase functions that can be calculated theoretically with codes like FEFF,[63] and $S_0^{\,2}$ is the amplitude reduction factor due to many-electronic effects. Equation 2 can be generalized to describe the contributions of MS paths as well, but in this case, A_p and φ_p will depend not only on the interatomic distances R but also on relative positions of the atoms (e.g., bonding angles).[66]

In a conventional ("quasi-harmonic") approach for EXAFS data analysis that works well for relatively ordered materials, $g_p(R)$ is expanded into cumulant series,[67] and after integration, one obtains the EXAFS equation in its commonly used form[43]

$$\chi_p(k) = \frac{S_0^{\,2} A_p(k) N_p}{\langle R\rangle_p^{\,2}} e^{-2k^2\sigma_p^{\,2}} \sin\!\left(2k\langle R\rangle_p - \frac{4}{3}\sigma_p^{(3)}k^3 + \varphi_p(k)\right) \tag{3}$$

which can be used for nonlinear least square-fitting of the experimental data. Here, N_p is the average coordination number, which for nanostructured samples can be linked to the NP size and shape,[43,68] $\langle R\rangle_p$ is the average interatomic distance, $\sigma_p^{\,2} = \sigma_{p,\,s}^{\,2} + \sigma_{p,\,T}^{\,2}$ is a disorder factor (mean square relative displacement (MSRD) in the bond-parallel direction, or Debye–Waller factor), which accounts for both the static disorder $\sigma_{p,\,s}^{\,2}$ (e.g., due to the relaxation of interatomic distances in near-surface layers) and thermal disorder due to thermal motion of atoms $\sigma_{p,\,T}^{\,2}$. The dependency of the latter on temperature T can be linked to the Debye temperature $\Theta_D = \hbar\omega_D/k_B$ in the material[69,70]

$$\sigma_T^{\,2} = \frac{\hbar}{M}\int_0^{\omega_D} \coth\!\left(\frac{\hbar\omega}{2k_BT}\right)\rho(\omega)\frac{d\omega}{\omega} \tag{4}$$

$$\rho(\omega) = \frac{3\omega^2}{\omega_D^3}\left(1 - \frac{\sin(\omega R/c)}{\omega R/c}\right) \tag{5}$$

where M is the atomic mass, R is the interatomic distance, $c = \omega_D/k_D$, $k_D = (6\pi^2 n/V)^{1/3}$, V/n is the crystal volume per atom, and k_B is Boltzmann's constant.

Finally, $\sigma_p^{(3)}$ is the third cumulant of the RDF and accounts for the skewness of the RDF peak. In principle, further terms from cumulant expansion can also be introduced into the EXAFS equation to account for increasingly more complex RDF shapes. However, in practice, these additional terms make EXAFS fitting unstable due to the correlations between different variables and the limited amount of information in the EXAFS data. The $\sigma_p^{(3)}$ term, nevertheless, is essential in studies of materials at high temperatures. Results of conventional EXAFS fitting in quasi-harmonic approximation are shown in Figure 2a for Pt NPs on SiO_2 in UHV and in Figure 3 for a Pt foil and for samples S2 and S3. Fitting was carried out following the protocol from ref 17, but the FEFF8 code[63] was used to model the A_p and φ_p functions, and the same fitting range in k space (between 2 and 11 Å^{-1}) was used for all samples and temperatures to propagate systematic errors in a similar way. The obtained values of structural parameters $\langle R\rangle$ and σ^2 for the first coordination shell are reported in Figure 2b,c. In addition, to illustrate the importance of non-Gaussian effects, in Figure 3a, we performed the fit of the temperature-dependent EXAFS spectra of a Pt foil in harmonic approximation (i.e., by setting $\sigma_p^{(3)}$ to 0). The obtained fits visually look almost as good as the fits in the quasi-harmonic approximation. However, the temperature dependence of the interatomic distances is strikingly different (see the inset in Figure 3a).

In particular, instead of the expansion expected for bulk platinum with increasing temperature, the Pt–Pt distances appear to be shrinking. This artifact is due to the increase in asymmetry of the Pt–Pt RDF and, hence, the increasing inaccuracy of the harmonic approximation at high temperatures. For the relatively ordered bulk Pt, inclusion of the third cumulant in the analysis allows us to fix this problem, but clearly, it cannot be considered a general solution, and for materials with larger disorder and more significant deviations in the shapes of the bond length distributions from Gaussian ones, even the quasi-harmonic approach will be inadequate and systematic errors in the values of structure parameters will be introduced.[53,54] It is therefore crucial in the analysis of the thermal expansion from EXAFS data to use methods that allow one to access the entire shape of the RDF.

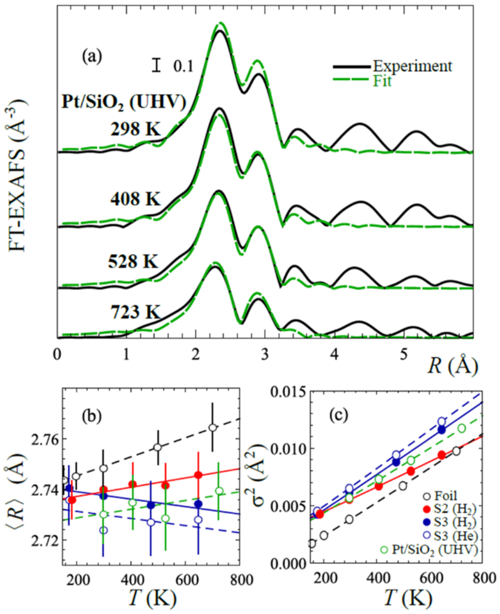

Figure 2. (a) Fourier transform (FT) EXAFS data for Pt NPs on SiO_2/Si(111) in UHV and results of conventional EXAFS data fitting in a quasi-harmonic approximation. (b) Average interatomic distances $\langle R\rangle$ and (c) disorder factors σ^2 for the first coordination shell, obtained in a quasi-harmonic EXAFS data fitting for a Pt foil and Pt NPs on SiO_2 and Al_2O_3 supports. Solid and dashed lines in panel (b) are linear fits of $\langle R\rangle(T)$ dependencies, and the results of the fitting of $\sigma^2(T)$ data by using the correlated Debye model (eqs 4 and 5) are shown in panel (c).

Another issue with probing thermal expansion via EXAFS analysis is that, normally, by thermal expansion, one understands the heating-induced changes in the material volume and lattice spacing, that is, in the distances between the average positions of atoms in the material R_{eq}, as probed, for example, by XRD methods. This is, however, not the same parameter that is directly probed by EXAFS. $\langle R\rangle$ in eq 2 is not the distance between average positions of atoms R_{eq} but rather an average bond length. Both are related as[47]

$$\langle R\rangle \approx R_{eq} + \langle \Delta u_\perp^{\,2}\rangle/(2R_{eq}) \tag{6}$$

where $\langle \Delta u_\perp^{\,2}\rangle$ is the MSRD component in the bond-perpendicular direction. Since $\langle \Delta u_\perp^{\,2}\rangle$ depends on the temperature analogously as σ^2 (MSRD in the bond-parallel direction), its changes will contribute to the temperature dependence of $\langle R\rangle$ and may, in fact, dominate over subtle thermal expansion-induced changes in R_{eq}. To distinguish between the disorder effects and the true thermal expansion, it may be therefore useful to consider the temperature-induced changes in interatomic distances in further coordination shells: Since the disorder contribution to the $\langle R\rangle$ value is inversely proportional to interatomic distance R_{eq}, it will be significantly suppressed for more distant coordination shells. It should be noted that $\langle \Delta u_\perp^{\,2}\rangle$ does not change significantly for different coordination shells for fcc metals, as can be verified by reverse Monte Carlo (RMC) simulations (see below). On the other

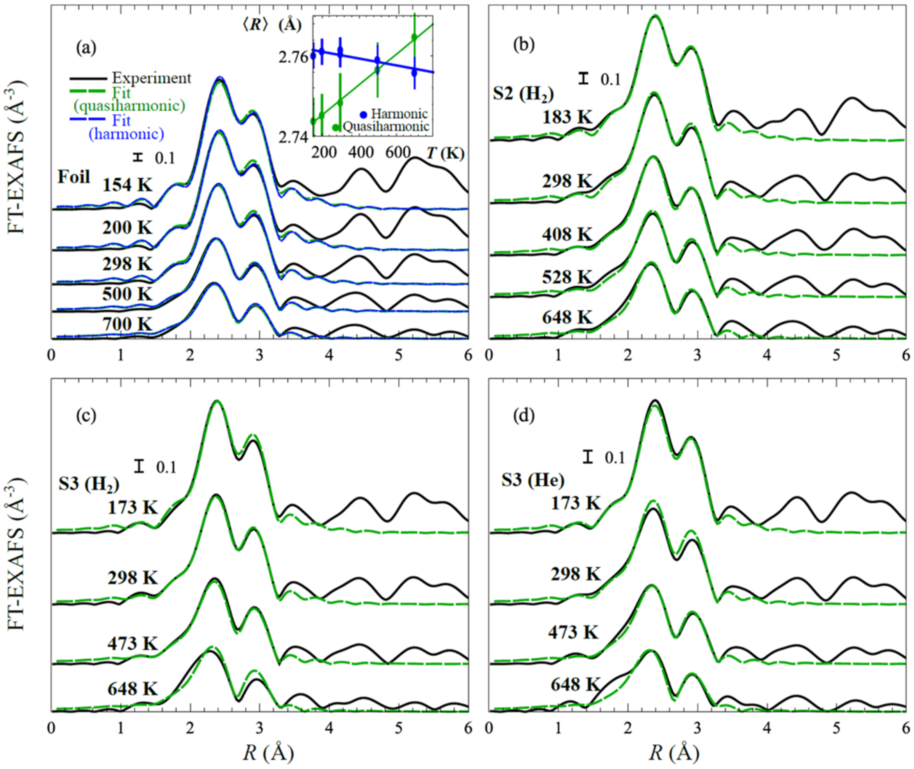

Figure 3. Fourier transform EXAFS data of a Pt foil measured in air (a) and of 0.8 nm (S3) and 1.0 nm (S2) Pt NPs on Al_2O_3 measured in H_2 (b,c) and He (S3) (d) atmospheres. Fitting is carried out in a quasi-harmonic approximation. For the Pt foil, results of fits conducted in the harmonic approximation are also shown. The obtained temperature dependences of the average interatomic distances in the harmonic and quasi-harmonic approximations for the Pt foil are compared in the inset in panel (a).

hand, the absolute value of the elongation of the interatomic distances due to the true thermal expansion is directly proportional to the interatomic distance; thus, for larger R_{eq} values, also larger (and thus more easily detectable) absolute changes upon temperature increase are expected. It is thus clear that access to interatomic distances in more distant coordination shells is beneficial for EXAFS-based studies of thermal expansion. Unfortunately, the accuracy of conventional approaches to EXAFS data analysis for the determination of structure parameters for coordination shells beyond the first one is usually very limited: contributions of distant coordination shells overlap strongly and overlap also with the contributions of MS paths, inducing strong correlations in the corresponding fitting variables.

For bulk materials with known densities and/or crystallographic structures, both, the problem of non-Gaussian bond length distributions and the problem of the analysis of distant coordination shells can be solved by RMC analysis where a 3D structure model of the material is constructed and atomic coordinates in the model are optimized in a random process, until a good agreement is obtained between experimental EXAFS spectrum and ab initio calculated EXAFS data for the structure model.[66,71,72] For nanomaterials, the RMC method is not immediately applicable because, for RMC simulations, knowledge of the initial structure model (e.g., number of atoms in the NP) is required, which is usually not available for NPs. At the same time, we have recently demonstrated that the same accuracy in the RDF determination as provided by the RMC method can be achieved by an NN-based approach,[61,62] which does not have such limitations for the analysis of EXAFS data of NPs.

Neural-Network-Based EXAFS Analysis. Our approach for NN-based EXAFS data analysis for NPs is described in detail and validated elsewhere.[62] In the former work, we have developed an NN suitable for the analysis of Pd K-edge and Au L_3-edge EXAFS data in PdAu NPs. Here, we developed a new NN with the same structure as previously used for the analysis of Au L_3-edge EXAFS data but now trained specifically for the analysis of Pt L_3-edge data in monometallic Pt NPs. Briefly, our NN is a composite function that can be represented as a network of nodes where nodes are arranged in several fully connected layers. The values of nodes in the input layer are initialized by the values of wavelet-transformed[73] EXAFS spectra. These values are further processed by the nodes in the following two hidden layers: each node in these layers adds with some weights the values of all nodes in the previous layer, applies an activation function (hyperbolic tangent) to the sum, and produces a single output, available for the nodes in the subsequent layer. The last layer in the NN is the output layer: the RDF is parametrized as a histogram with bin size ΔR, and the value of each node in the NN output layer corresponds to the height of a certain RDF histogram bin. The minimal bin size is limited by the length of the available EXAFS spectra in k space: $\Delta R = 1/(2k_{max} - 2k_{min})$.[74]

During the NN training step, the weights of all nodes in the NN are optimized to ensure correct mapping of the EXAFS features to shapes of the RDF peaks. For this purpose, we use a large set of training examples (ca. 50000 in this case): theoretical EXAFS spectra for which we know the corresponding true values of the RDFs. Such theoretical EXAFS spectra are obtained in MD simulations with an empirical Sutton—Chen potential[66,75,76] at different temperatures for Pt NPs with different sizes, shapes, and crystallographic structures. Such MD simulations yield realistically disordered NPs structures, are in a good agreement with experimental data both for bulk and nanomaterials,[54,62,66,77] and thus are suitable for NN training. After the NN training is completed, the NN weights are fixed and the NN can process experimental EXAFS data, yielding corresponding RDF values. As in our previous works,[61,62,78] to estimate statistical uncertainties, we construct and train five different NNs using different initializations of the NN node weights and different subsets of the training data set. The RDFs reported in this work are the average result of these five NNs. The standard deviations of the NNs predictions are used to estimate the statistical errors of the structural parameters. Unlike RMC, the NN-EXAFS method is not biased by the choice of the initial structure model, it yields physically reasonable RDF (because realistic RDFs are used for NN training), it can be used for analysis of EXAFS data with a limited k range (a k range between 3 and 11 $Å^{-1}$ is used in this work, which is typical for in situ EXAFS studies), and it is also very quick. After the NN training is completed, an unlimited number of spectra can be processed within seconds, while, for comparison, RMC simulations take several CPU days for each spectrum. See ref 62 for more technical details on NN training and implementation.

An important difference between the NN used in this work and the previous implementation of the NN method in ref 62 is the treatment of the correction to the photoelectron reference energy ΔE_0. Note that the E_0 value in eq 1 can change from sample to sample due to, for example, charge transfer between different parts of a multicomponent material. Importantly, previous experimental and theoretical studies report that the E_0 value may change also with temperature[14,17,40] (by around 1−1.5 eV). This is a severe problem for studies of thermal expansion with the EXAFS method because changes in the E_0 value can mask the effect of changes in bond length distributions. To avoid that, here, we propose a simple solution: to disentangle the effects of the ΔE_0 and RDF shape in the NN analysis, during the NN training, each of the ~50000 training EXAFS spectra is artificially shifted by a random ΔE_0 value. In this way, we ensure that the NN does not assign any physical meaning to a small shift of the energy scale in experimental EXAFS data. The importance and success of this solution are demonstrated in the Supporting Information (Note S1 and Figure S3).

To validate the accuracy of this NN for materials with various degrees of disorder and with different interatomic distances, we compare the results yielded by the NN with the results of RMC simulations for experimental EXAFS data for bulk Pt at different temperatures (Figures 4 and 5). Note also that, while our NN was trained on theoretical EXAFS data for Pt only, it can be applied to analyze EXAFS data of elements that are neighbors of Pt in the Periodic Table (Ir and Au).[61,62] Results of RMC simulations for Au and Ir foils are therefore also shown in Figures 4 and 5. The reason that allows us to use here RMC as a standard to assess the accuracy of the NN method is that the quality of the RMC model can be immediately verified by directly comparing experimental EXAFS data with theoretical EXAFS spectra calculated for the final RMC structure model (Figure 4). A comparison of the RDFs yielded by the RMC and NN approaches for bulk materials is shown in Figure 5. See refs 54, 62, and 78 for the details of RMC calculations.

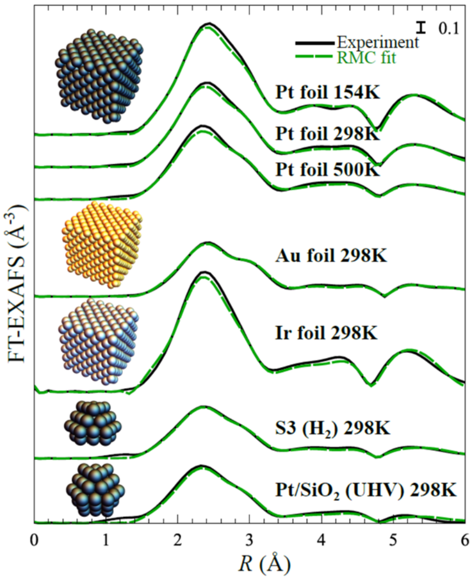

Figure 4. Comparison of Fourier transform (FT) experimental EXAFS data and theoretical EXAFS spectra obtained in RMC simulations for a Pt foil at different temperatures, as well as for Au and Ir foils at room temperature. Results for Pt NPs (sample S3 on Al_2O_3 in a H_2 atmosphere and Pt/SiO_2 sample in UHV) are also shown. EXAFS spectra are shifted vertically for clarity. Insets show the final structure models, obtained in the RMC simulations for the corresponding material at room temperature (note that, for bulk materials, periodic boundary conditions were used in the RMC simulations).

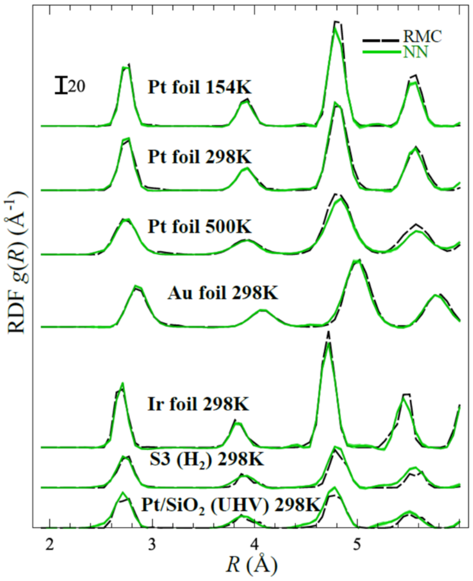

Figure 5. Comparison of RDFs, obtained from RMC simulations and from NN-EXAFS analysis for reference materials. The RDFs are shifted vertically for clarity.

As mentioned above, applicability of the RMC method to the analysis of EXAFS data in NPs is limited. Nevertheless, for selected model material systems, RMC modeling can be carried out if the approximate structure model of the NPs can be independently obtained. In our previous works, we were able to construct such structure models for Pt/SiO_2 NPs in UHV,[64] as well as for sample S3 in H_2,[78] using information from the analysis of XANES data, conventional EXAFS analysis, and microscopy data. These structural models were further refined via an RMC procedure, and a good agreement between experimental and modeled EXAFS data was obtained (Figure 4). In Figure 5, we compare the RDFs, obtained in such RMC calculations, with the NN-EXAFS results to demonstrate the accuracy of our NN not only for bulk but also for nanosized materials. The trained and validated NN can be then applied to analyze experimental temperature-dependent EXAFS data in Pt NPs on various supports, with different particle sizes and in different atmospheres. The obtained RDFs are summarized in Figure 6.

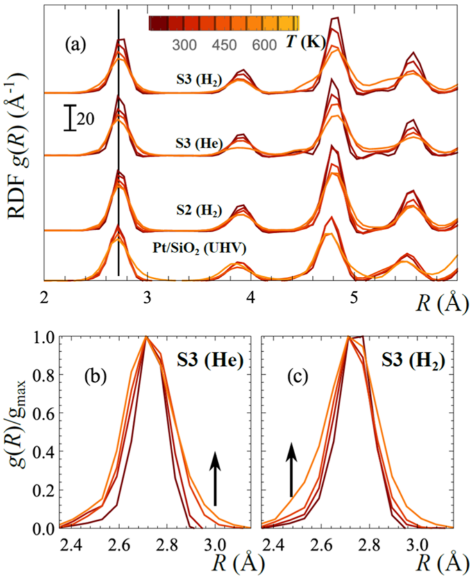

Figure 6. Temperature-dependent RDFs, yielded by the NN-EXAFS method for Al_2O_3-supported S2 and S3 samples (0.8−1 nm Pt NPs), as well as for SiO_2-supported Pt NPs (1−2 nm) measured in UHV. For clarity, the RDFs are shifted vertically in panel (a). A vertical line shows the position of the first RDF peak, corresponding to the first coordination shell. Panels (b) and (c) show zoomed-in first shell RDFs for sample S3 in He (b) and H_2 (c) atmospheres. For clarity, the RDFs in panels (b) and (c) are normalized by dividing them by g_{max}, the maximal RDF value in the range between 2.4 and 3.2 Å. Arrows indicate the direction of the most pronounced temperature-induced change in the shape of the RDF peak.

Finally, for quantitative analysis of thermal properties of NPs, one can calculate the average interatomic distance $\langle R\rangle_p = \frac{1}{N_p}\int_{R_1^p}^{R_2^p} g_p(R)R\,\mathrm{d}R$, where N_p is the average coordination number $N_p = \int_{R_1^p}^{R_2^p} g_p(R)\,\mathrm{d}R$, and the integration limits R_1^p and R_2^p are chosen so that the contribution of only the coordination shell of interest is considered.[61,62] Similarly, the disorder factor $\sigma_p{}^2$ can be calculated as $\sigma_p{}^2 = \frac{1}{N_p}\int_{R_1^p}^{R_2^p} g_p(R)(R - \langle R\rangle_p)^2\,\mathrm{d}R$. Note that this definition allows us to avoid also the ambiguities related to the choice of $S_0{}^2$ (see eqs 2 and 3). Here, the chosen $S_0{}^2$ value directly affects the values of the coordination numbers N_p but cancels out in the definitions of $\langle R\rangle_p$ and $\sigma_p{}^2$ since both N_p and $g_p(R)$ are inversely proportional to $S_0{}^2$. The temperature dependencies of $\langle R\rangle_p$ and $\sigma_p{}^2$, obtained by integration of the RDFs yielded by NN for a Pt foil and Pt NPs, are compared in Figure 7.

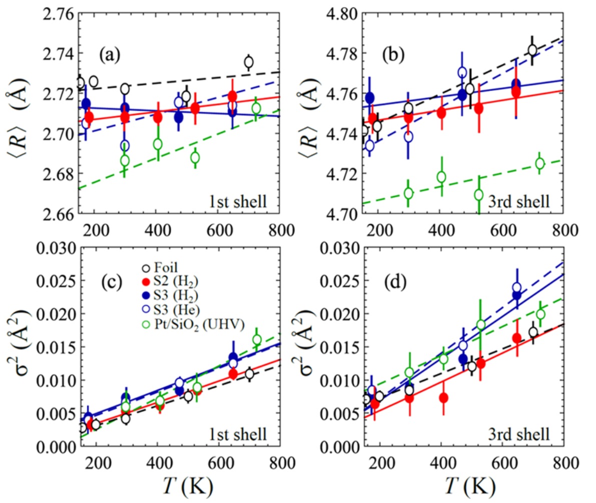

Figure 7. Average interatomic distances ⟨R⟩ (a,b) and σ^2 factors (c,d) for the first (a,c) and third (b,d) coordination shells obtained by the integration of the RDFs yielded by the NN-EXAFS analysis of a Pt foil and of micellar Pt NPs on SiO_2 and Al_2O_3 supports. Solid and dashed lines are linear fits of $\langle R\rangle(T)$ dependences in (a,b), and results of the fitting of $\sigma^2(T)$ data by the correlated Debye model (eqs 4 and 5) (c,d).

■ DISCUSSION

The first step in studies of size-dependent thermal properties in NPs is to verify that the particle size does not change during the experiment. Here and in our previous works, the stability of the NPs is achieved through a high-temperature annealing pretreatment. In this case, all irreversible temperature-induced changes in the NP structure already took place before XAS data collection, which was done up to a lower maximum temperature than that used for the pretreatment. As was previously shown,[78] Pt L_3-edge XANES data are a sensitive probe of the NP size and shape. Therefore, the lack of temperature-induced changes in the XANES features (Figure 1) demonstrates clearly that the NP morphology is preserved during our experiments. Note also that, in Figure 1, we observe no changes in the position of the absorption edge (E_0 value) in our data for SiO_2-supported Pt NPs in UHV, in contrast to the previous findings for Al_2O_3-supported[14,17,40] and SiO_2-supported NPs in helium and hydrogen.[79] This suggests that the temperature dependence of E_0 discussed above is strongly system-specific and is affected by support and adsorbates.

Next, we turn to the analysis of EXAFS data. The results of conventional EXAFS data fitting (Figure 2b,c) are in good agreement with the previous report.[17] The temperature dependence of the interatomic distance appears to have a negative slope for the Al_2O_3-supported Pt NPs in sample S3 in H_2 and He and has a positive but lower slope than that of bulk Pt for the Al_2O_3-supported Pt NPs in sample S2 in H_2 (Figure 2b). As mentioned above, in our previous work, the suppressed or even negative thermal expansion of bond lengths for these samples was partially explained by temperature-dependent hydrogen coverage (the effect of hydrogen coverage on interatomic distances can be clearly seen in Figure 2 by comparing results for S3 in H_2 and He atmospheres).This argument, however, does not explain why NTE is also observed for this sample in He. Similarly, for our new sample (Pt/SiO_2 in UHV), the slope of the temperature dependence of the Pt−Pt bond lengths is positive but appears to be suppressed in comparison to that of bulk Pt, even in the absence of any adsorbates. Finally, when temperature dependencies of the Debye−Waller factors σ^2 are considered, conventional EXAFS analysis results, summarized in Figure 2c, show that for sample S3 the slope of the $\sigma^2(T)$ function is similar to that of the Pt foil, but it is noticeably reduced for S2 and for Pt/SiO_2 in UHV. Since the slope of the $\sigma^2(T)$ function in the high-temperature regime is inversely proportional to the Debye temperature squared,[19,70,80] this result implies that the Debye temperature is anomalously low for these two samples.

To determine whether the observed anomalies are of physical nature or are artifacts of the conventional EXAFS analysis procedure, we now focus on the results obtained by the neural network method. As suggested from the good agreement between RMC and NN results for reference materials (Figures 4 and 5), the accuracy of our NN approach is sufficient to detect reliably the changes in the RDFs in a broad range of temperatures and particle sizes. Temperature-dependent RDFs for Pt NPs are compared in Figure 6. As expected, the NN shows that, with increasing temperature, all RDF peaks broaden, in agreement with an increase in thermal disorder. NN results show no obvious changes in the RDF peak positions with temperature. Nevertheless, the asymmetry of the RDF peaks and deviations from the Gaussian shape get more pronounced at higher temperatures. This immediately indicates that the results of conventional analysis should be considered with caution for this system because the possibility to account for these non-Gaussian shapes of bond length distributions is limited in the conventional approach. Moreover, as better shown in Figure 6b,c, the evolution of the RDF peak shape depends on the sample environment. While, for the S3 sample in He (and also for Pt/SiO_2 in UHV), the RDF peaks get positively skewed with increasing temperature (as expected for increasingly anharmonic thermal motion of atoms), for the same sample in H_2 the RDF peak, corresponding to the first coordination shell, appears to be rather negatively skewed at higher temperature. This peculiar evolution of the RDF peak shape for sample S3 in H_2 may be interpreted as an indication that it is significantly affected by the changes in the static disorder contribution upon changes in temperature (e.g., due to temperature-driven desorption of hydrogen species and the following structure relaxation).[19]

For quantitative analysis, we integrated the RDF peaks to calculate average interatomic distances and disorder factors (Figure 7). We limit our discussion to the first and third coordination shells here because the corresponding RDF peaks remain well-defined at all temperatures and for all samples and we can choose the integration limits so that the contribution of other coordination shells is not significant. Temperature dependencies of the interatomic distances in the first coordination shell are shown in Figure 7a. As one can see, after non-Gaussian shapes of bond length distributions are taken into account, the temperature dependencies of the Pt−Pt bond lengths in all hydrogen-free samples (Pt/SiO_2 in UHV and S3 in He) show no signs of negative or even suppressed thermal expansion: the slopes of $\langle R\rangle(T)$ are even larger than that for bulk Pt, which can be a signature of enhanced thermal expansion but, more likely, is a result of an increase in the thermal disorder ($\langle\Delta u_\perp{}^2\rangle$ term in eq 6). For both samples in a H_2 atmosphere (S2 and S3), the change of the bond lengths upon temperature increase, nevertheless, is noticeably suppressed and is close to 0 or even slightly negative (for S3 sample). To better distinguish between disorder-induced effects and intrinsic thermal expansion, we now turn to the analysis of the bond lengths in the third coordination shell (Figure 7b). As discussed above, the intrinsic NTE should be more pronounced in the contributions of distant coordination shells. The situation, however, is exactly the opposite in Figure 7b. Even for sample S3 in H_2, where the shortening of the Pt−Pt distance in the 1st coordination shell was observed in Figure 7a, the Pt−Pt distance in the third coordination shell increases with temperature. Therefore, we can conclude that the observed shortening of the nearest-neighbor distance in the Pt NPs in a H_2 atmosphere is a local effect related to the temperature-dependent hydrogen coverage and its influence on the bond length disorder, in agreement with the previous DFT-based studies.[19] To explain the difference between the trends in the interatomic distances for the first and third coordination shells for the S3 sample in hydrogen, one can note that, in Figure 6a, the shape of the third RDF peak is getting positively skewed with increasing temperature for this sample (as well as all others), indicating that the thermal contribution to disorder factors dominates over the surface-induced static disorder effects for the third coordination shell. According to eq 6, the difference in the disorder trends for the first and third coordination shells can also result in the differences in the changes in interatomic distances upon heating, leading to an apparent shrinking of bond lengths in the first coordination shell but expansion of the interatomic distances in the third coordination shell. Importantly, such a difference between the first and third coordination shells is not observed for any of our samples measured in the absence of hydrogen (in He or UHV conditions) where only the expansion of the interatomic distances upon heating is observed. This gives us confidence that the observed anomalous behavior of sample S3 in hydrogen is a direct consequence of the interactions between Pt NPs and hydrogen adsorbates.

Finally, when the temperature dependencies of the disorder factors σ^2 are considered (Figure 7c,d), our results obtained by the NN method show that no anomalies in the slopes of $\sigma^2(T)$ can be observed when non-Gaussian effects are taken into account. For instance, in the first coordination shell, for all samples, the slopes of $\sigma^2(T)$ are very similar to that in bulk Pt, and the corresponding Debye temperatures (ca. 225 K for S3 sample both in H_2 and He atmospheres, 237 K for S2 sample, 194 K for Pt/SiO_2 in UHV) are close and/or lower than that for bulk Pt (244 K). The contribution of static disorder seems to be relatively small in all samples, but it is slightly larger in sample S3, as evidenced by the vertical offset of $\sigma^2(T)$ for this sample. Similar conclusions can be drawn also from the examination of $\sigma^2(T)$ trends for the third coordination shell: for all NP samples, the slopes of $\sigma^2(T)$ are larger than that of bulk Pt, with the corresponding effective Debye temperatures of 162−169 (for S3 sample in H_2 and He atmospheres) and 204 K (both for S2 in H_2 and Pt/SiO_2 in UHV) being smaller than 220 K for bulk Pt. The particularly reduced effective Debye temperature in the S3 sample can be related to the very small particle size in this sample (ca. 0.8 nm), in agreement with the predictions of theoretical models. It should be noted that the considerations discussed above apply to Pt NPs with relatively weak interactions with the support (NP intrinsic effect), as yielded by our synthesis method. Alternative Pt NP synthesis procedures such as incipient wetness impregnation[14] can result in significantly flatter NP shapes with higher contact area with the support.[78] In such cases, particle-support interactions can have a critical effect on the properties of the NPs, resulting in significantly more disordered structures, and a possible shrinking of interatomic distances upon heating even in an inert atmosphere, as has been previously reported.[14,15] Nonetheless, accounting for non-Gaussian shapes of bond length distributions in such systems is still equally important for the correct interpretation of the EXAFS data from these systems. Furthermore, the detailed analysis of the role of the NP shape and particle-support interactions on the asymmetry of the RDFs and thermal properties of metal NPs deserves further investigation.

■ CONCLUSIONS

By carefully accounting for systematic errors and employing advanced approaches for EXAFS data analysis based on the use of an artificial neural network method, we were able to resolve a long-standing controversy regarding seemingly anomalous thermal properties of supported metal NPs. The results obtained were further supported by the analysis of new in situ EXAFS data collected for Pt NPs in ultrahigh vacuum. We have demonstrated that the previously observed shortening in the Pt−Pt distance in small, preformed NPs upon temperature increase is not due to an intrinsic NTE but is rather a local effect due to temperature-dependent hydrogen coverage and corresponding changes in the local static disorder. For preformed NP samples without hydrogen adsorbates and strong NP-support interaction, temperature-driven shortening of Pt−Pt distances is not observed in EXAFS data, as long as non-Gaussian shapes of bond length distributions are properly taken into account. We also demonstrated that the previously reported anomalously large Debye temperatures for Pt NPs are a similar artifact of conventional EXAFS data analysis. If deviations from Gaussian shapes are considered, as made possible here by employing the NN method, giving a more realistic description of these complex nanoscale systems, the Debye temperatures for all NPs samples are lower than that of bulk Pt. Our results thus clarify the intrinsic thermodynamics properties of small supported metal NPs. At the same time, we show that conventional approaches to EXAFS data analysis need to be used with caution when applied to in situ studies of disordered systems such as small nanoparticles in contact with a support and/or adsorbates and materials at high temperature. Advanced approaches such as neural-network-based analysis may be much better suited for these applications.

■ ASSOCIATED CONTENT

Ⓢ Supporting Information

The Supporting Information is available free of charge on the ACS Publications website at DOI: 10.1021/acs.jpcc.9b05037.

> AFM image of Pt NPs on single-crystal $SiO_2/Si(111)$ support, experimental EXAFS data in k space for Pt NPs on single-crystal $SiO_2/Si(111)$ support and on Al_2O_3 support, discussion of the effect of the E_0 value in neural-network-based EXAFS analysis, and the importance of this effect and success of our approach to address this problem (PDF)

■ AUTHOR INFORMATION

Corresponding Author
*E-mail: roldan@fhi-berlin.mpg.de.

ORCID
Beatriz Roldan Cuenya: 0000-0002-8025-307X

Notes

The authors declare no competing financial interest.

■ ACKNOWLEDGMENTS

This work was funded by the European Research Council (ERC-725915, OPERANDOCAT) and the U.S. National Science Foundation (NSF-CHEM-1213182 and NSF- DMR-1207065). The authors are grateful to Dr. H. Mistry, Dr. L. R. Merte, and Dr. F. Behafarid for assistance during the in situ XAS measurements, and to Prof. Anatoly Frenkel for insightful discussions. RMC-EXAFS and MD-EXAFS simulations were performed on the LASC cluster-type computer at the Institute of Solid State Physics of the University of Latvia.

■ REFERENCES

(1) Halperin, W. P. Quantum size effects in metal particles. *Rev. Mod. Phys.* **1986**, *58*, 533−606.

(2) De Heer, W. A. The physics of simple metal clusters: experimental aspects and simple models. *Rev. Mod. Phys.* **1993**, *65*, 611−676.

(3) Roldan Cuenya, B. Synthesis and catalytic properties of metal nanoparticles: Size, shape, support, composition, and oxidation state effects. *Thin Solid Films* **2010**, *518*, 3127−3150.

(4) Balerna, A.; Bernieri, E.; Picozzi, P.; Reale, A.; Santucci, S.; Burattini, E.; Mobilio, S. Extended X-ray-absorption fine-structure and near-edge-structure studies on evaporated small clusters of Au. *Phys. Rev. B* **1985**, *31*, 5058−5065.

(5) Zanchet, D.; Tolentino, H.; Alves, M. M. C.; Alves, O.; Ugarte, D. Inter-atomic distance contraction in thiol-passivated gold nanoparticles. *Chem. Phys. Lett.* **2000**, *323*, 167−172.

(6) Huang, W. J.; Sun, R.; Tao, J.; Menard, L. D.; Nuzzo, R. G.; Zuo, J. M. Coordination-dependent surface atomic contraction in nanocrystals revealed by coherent diffraction. *Nat. Mater.* **2008**, *7*, 308.

(7) Solliard, C.; Flueli, M. Surface stress and size effect on the lattice parameter in small particles of gold and platinum. *Surf. Sci.* **1985**, *156*, 487−494.

(8) Buffat, P.; Borel, J. P. Size effect on the melting temperature of gold particles. *Phys. Rev. A* **1976**, *13*, 2287−2298.

(9) Yang, C. C.; Xiao, M. X.; Li, W.; Jiang, Q. Size effects on Debye temperature, Einstein temperature, and volume thermal expansion coefficient of nanocrystals. *Solid State Commun.* **2006**, *139*, 148−152.

(10) Zhao, Y. H.; Lu, K. Grain-size dependence of thermal properties of nanocrystalline elemental selenium studied by x-ray diffraction. *Phys. Rev. B* **1997**, *56*, 14330−14337.

(11) Hou, M.; El Azzaoui, M.; Pattyn, H.; Verheyden, J.; Koops, G.; Zhang, G. Growth and lattice dynamics of Co nanoparticles embedded in Ag: a combined molecular-dynamics simulation and Mössbauer study. *Phys. Rev. B* **2000**, *62*, 5117−5128.

(12) Childress, J. R.; Chien, C. L.; Zhou, M. Y.; Sheng, P. Lattice softening in nanometer-size iron particles. *Phys. Rev. B* **1991**, *44*, 11689−11696.

(13) Lai, S. L.; Guo, J. Y.; Petrova, V.; Ramanath, G.; Allen, L. H. Size-dependent melting properties of small tin particles: nanocalorimetric measurements. *Phys. Rev. Lett.* **1996**, *77*, 99−102.

(14) Sanchez, S. I.; Menard, L. D.; Bram, A.; Kang, J. H.; Small, M. W.; Nuzzo, R. G.; Frenkel, A. I. The emergence of nonbulk properties in supported metal clusters: negative thermal expansion and atomic disorder in Pt nanoclusters supported on γ-Al_2O_3. *J. Am. Chem. Soc.* **2009**, *131*, 7040−7054.

(15) Kang, J. H.; Menard, L. D.; Nuzzo, R. G.; Frenkel, A. I. Unusual non-bulk properties in nanoscale materials: thermal metal− metal

bond contraction of γ-alumina-supported Pt catalysts. *J. Am. Chem. Soc.* **2006**, *128*, 12068−12069.

(16) Giulian, R.; Araujo, L. L.; Kluth, P.; Sprouster, D. J.; Schnohr, C. S.; Foran, G. J.; Ridgway, M. C. Temperature-dependent EXAFS analysis of embedded Pt nanocrystals. *J. Phys.: Condens. Matter* **2009**, *21*, 155302.

(17) Roldan Cuenya, B.; Frenkel, A. I.; Mostafa, S.; Behafarid, F.; Croy, J. R.; Ono, L. K.; Wang, Q. Anomalous lattice dynamics and thermal properties of supported size- and shape-selected Pt nanoparticles. *Phys. Rev. B* **2010**, *82*, 155450.

(18) Araujo, L. L.; Kluth, P.; de M. Azevedo, G.; Ridgway, M. C. Vibrational properties of Ge nanocrystals determined by EXAFS. *Phys. Rev. B* **2006**, *74*, 184102.

(19) Roldan Cuenya, B.; Alcántara Ortigoza, M.; Ono, L. K.; Behafarid, F.; Mostafa, S.; Croy, J. R.; Paredis, K.; Shafai, G.; Rahman, T. S.; Li, L.; Zhang, Z.; Yang, J. C. Thermodynamic properties of Pt nanoparticles: Size, shape, support, and adsorbate effects. *Phys. Rev. B* **2011**, *84*, 245438.

(20) Fecht, H. J. Intrinsic instability and entropy stabilization of grain boundaries. *Phys. Rev. Lett.* **1990**, *65*, 610−613.

(21) Leontyev, I. N.; Kulbakov, A. A.; Allix, M.; Rakhmatullin, A.; Kuriganova, A. B.; Maslova, O. A.; Smirnova, N. V. Thermal expansion coefficient of carbon-supported Pt nanoparticles: In-situ X-ray diffraction study. *Phys. Status Solidi B* **2017**, *254*, 1600695.

(22) Zhu, Y. F.; Lian, J. S.; Jiang, Q. Modeling of the melting point, Debye temperature, thermal expansion coefficient, and the specific heat of nanostructured materials. *J. Phys. Chem. C* **2009**, *113*, 16896−16900.

(23) Hansen, P. L.; Wagner, J. B.; Helveg, S.; Rostrup-Nielsen, J. R.; Clausen, B. S.; Topsøe, H. Atom-resolved imaging of dynamic shape changes in supported copper nanocrystals. *Science* **2002**, *295*, 2053−2055.

(24) Lee, J.-G.; Mori, H. Solid solubility in isolated nanometer-sized alloy particles in the Sn-Pb system. *Eur. Phys. J. D* **2005**, *34*, 227−230.

(25) Li, W.-H.; Wu, S. Y.; Yang, C. C.; Lai, S. K.; Lee, K. C.; Huang, H. L.; Yang, H. D. Thermal contraction of Au nanoparticles. *Phys. Rev. Lett.* **2002**, *89*, 135504.

(26) Comaschi, T.; Balerna, A.; Mobilio, S. Temperature dependence of the structural parameters of gold nanoparticles investigated with EXAFS. *Phys. Rev. B* **2008**, *77*, No. 075432.

(27) Frenkel, A. I.; Vasić, R.; Dukesz, B.; Li, D.; Chen, M.; Zhang, L.; Fujita, T. Thermal properties of nanoporous gold. *Phys. Rev. B* **2012**, *85*, 195419.

(28) Mary, T. A.; Evans, J. S. O.; Vogt, T.; Sleight, A. W. Negative thermal expansion from 0.3 to 1050 Kelvin in ZrW_2O_8. *Science* **1996**, *272*, 90−92.

(29) Goodwin, A. L.; Calleja, M.; Conterio, M. J.; Dove, M. T.; Evans, J. S. O.; Keen, D. A.; Peters, L.; Tucker, M. G. Colossal positive and negative thermal expansion in the framework material $Ag_3[Co(CN)_6]$. *Science* **2008**, *319*, 794−797.

(30) Goodwin, A. L.; Kepert, C. J. Negative thermal expansion and low-frequency modes in cyanide-bridged framework materials. *Phys. Rev. B* **2005**, *71*, 140301.

(31) Perottoni, C. A.; da Jornada, J. A. H. Pressure-induced amorphization and negative thermal expansion in ZrW_2O_8. *Science* **1998**, *280*, 886−889.

(32) Ernst, G.; Broholm, C.; Kowach, G. R.; Ramirez, A. P. Phonon density of states and negative thermal expansion in ZrW_2O_8. *Nature* **1998**, *396*, 147−149.

(33) Salvador, J. R.; Guo, F.; Hogan, T.; Kanatzidis, M. G. Zero thermal expansion in YbGaGe due to an electronic valence transition. *Nature* **2003**, *425*, 702−705.

(34) Ramirez, A. P.; Kowach, G. R. Large low temperature specific heat in the negative thermal expansion CompoundZrW2O8. *Phys. Rev. Lett.* **1998**, *80*, 4903−4906.

(35) Azuma, M.; Chen, W.-t.; Seki, H.; Czapski, M.; Olga, S.; Oka, K.; Mizumaki, M.; Watanuki, T.; Ishimatsu, N.; Kawamura, N.; Ishiwata, S.; Tucker, M. G.; Shimakawa, Y.; Attfield, J. P. Colossal negative thermal expansion in $BiNiO_3$ induced by intermetallic charge transfer. *Nat. Commun.* **2011**, *2*, 347.

(36) Chen, J.; Hu, L.; Deng, J.; Xing, X. Negative thermal expansion in functional materials: controllable thermal expansion by chemical modifications. *Chem. Soc. Rev.* **2015**, *44*, 3522−3567.

(37) Barrera, G. D.; Bruno, J. A. O.; Barron, T. H. K.; Allan, N. L. Negative thermal expansion. *J. Phys.: Condens. Matter* **2005**, *17*, R217.

(38) White, G. K. Solids: thermal expansion and contraction. *Contemp. Phys.* **2006**, *34*, 193−204.

(39) Zheng, X. G.; Kubozono, H.; Yamada, H.; Kato, K.; Ishiwata, Y.; Xu, C. N. Giant negative thermal expansion in magnetic nanocrystals. *Nat. Nanotechnol.* **2008**, *3*, 724.

(40) Vila, F.; Rehr, J. J.; Kas, J.; Nuzzo, R. G.; Frenkel, A. I. Dynamic structure in supported Pt nanoclusters: real-time density functional theory and X-ray spectroscopy simulations. *Phys. Rev. B* **2008**, *78*, 121404.

(41) Oudenhuijzen, M. K.; Bitter, J. H.; Koningsberger, D. C. The nature of the Pt− H bonding for strongly and weakly bonded hydrogen on platinum. A XAFS spectroscopy study of the Pt− H antibonding shaperesonance and Pt− H EXAFS. *J. Phys. Chem. B* **2001**, *105*, 4616−4622.

(42) Rehr, J. J.; Albers, R. C. Theoretical approaches to X-ray absorption fine structure. *Rev. Mod. Phys.* **2000**, *72*, 621−654.

(43) Frenkel, A. I. Applications of extended X-ray absorption fine-structure spectroscopy to studies of bimetallic nanoparticle catalysts. *Chem. Soc. Rev.* **2012**, *41*, 8163−8178.

(44) Frenkel, A. I.; Hills, C. W.; Nuzzo, R. G. A view from the inside: complexity in the atomic scale ordering of supported metal nanoparticles. *J. Phys. Chem. B* **2001**, *105*, 12689−12703.

(45) Frenkel, A. I.; Yevick, A.; Cooper, C.; Vasic, R. Modeling the structure and composition of nanoparticles by extended X-ray absorption fine-structure spectroscopy. *Annu. Rev. Anal. Chem.* **2011**, *4*, 23−39.

(46) Frenkel, A. I.; Rehr, J. J. Thermal expansion and X-ray-absorption fine-structure cumulants. *Phys. Rev. B* **1993**, *48*, 585−588.

(47) Dalba, G.; Fornasini, P.; Grisenti, R.; Purans, J. Sensitivity of extended X-ray-absorption fine structure to thermal expansion. *Phys. Rev. Lett.* **1999**, *82*, 4240−4243.

(48) Fornasini, P.; a Beccara, S.; Dalba, G.; Grisenti, R.; Sanson, A.; Vaccari, M.; Rocca, F. Extended X-ray-absorption fine-structure measurements of copper: Local dynamics, anharmonicity, and thermal expansion. *Phys. Rev. B* **2004**, *70*, 174301.

(49) Clausen, B. S.; Grabaek, L.; Topsoe, H.; Hansen, L. B.; Stoltze, P.; Norskov, J. K.; Nielsen, O. H. A new procedure for particle size determination by EXAFS based on molecular dynamics simulations. *J. Catal.* **1993**, *141*, 368−379.

(50) Clausen, B. S.; Topsøe, H.; Hansen, L. B.; Stoltze, P.; Nørskov, J. K. Determination of metal particle sizes from EXAFS. *Catal. Today* **1994**, *21*, 49−55.

(51) Clausen, B. S.; Norskov, J. K. Asymmetric pair distribution functions in catalysts. *Top. Catal.* **2000**, *10*, 221−230.

(52) Hansen, L. B.; Stoltze, P.; Nørskov, J. K.; Clausen, B. S.; Niemann, W. Is there a contraction of the interatomic distance in small metal particles? *Phys. Rev. Lett.* **1990**, *64*, 3155−3158.

(53) Chill, S. T.; Anderson, R. M.; Yancey, D. F.; Frenkel, A. I.; Crooks, R. M.; Henkelman, G. Probing the limits of conventional extended X-ray absorption fine structure analysis using thiolated gold nanoparticles. *ACS Nano* **2015**, *9*, 4036−4042.

(54) Timoshenko, J.; Frenkel, A. I. Probing structural relaxation in nanosized catalysts by combining EXAFS and reverse Monte Carlo methods. *Catal. Today* **2017**, *280*, 274−282.

(55) Yancey, D. F.; Chill, S. T.; Zhang, L.; Frenkel, A. I.; Henkelman, G.; Crooks, R. M. A theoretical and experimental examination of systematic ligand-induced disorder in Au dendrimer-encapsulated nanoparticles. *Chem. Sci.* **2013**, *4*, 2912−2921.

(56) Yevick, A.; Frenkel, A. I. Effects of surface disorder on EXAFS modeling of metallic clusters. *Phys. Rev. B* **2010**, *81*, 115451.

(57) Eisenberger, P.; Brown, G. S. The study of disordered systems by EXAFS: limitations. *Solid State Commun.* **1979**, *29*, 481−484.

(58) Vila, F. D.; Rehr, J. J.; Nuzzo, R. G.; Frenkel, A. I. Anomalous Structural Disorder in Supported Pt Nanoparticles. *J. Phys. Chem. Lett.* **2017**, *8*, 3284−3288.

(59) Kästle, G.; Boyen, H.-G.; Weigl, F.; Lengl, G.; Herzog, T.; Ziemann, P.; Riethmüller, S.; Mayer, O.; Hartmann, C.; Spatz, J. P.; Möller, M.; Ozawa, M.; Banhart, F.; Garnier, M. G.; Oelhafen, P. Micellar nanoreactors—preparation and characterization of hexagonally ordered arrays of metallic nanodots. *Adv. Funct. Mater.* **2003**, *13*, 853−861.

(60) Ono, L. K.; Yuan, B.; Heinrich, H.; Roldan Cuenya, B. Formation and thermal stability of platinum oxides on size-selected platinum nanoparticles: support effects. *J. Phys. Chem. C* **2010**, *114*, 22119−22133.

(61) Timoshenko, J.; Anspoks, A.; Cintins, A.; Kuzmin, A.; Purans, J.; Frenkel, A. I. Neural network approach for characterizing structural transformations by X-ray absorption fine structure spectroscopy. *Phys. Rev. Lett.* **2018**, *120*, 225502.

(62) Timoshenko, J.; Wrasman, C. J.; Luneau, M.; Shirman, T.; Cargnello, M.; Bare, S. R.; Aizenberg, J.; Friend, C. M.; Frenkel, A. I. Probing atomic distributions in mono- and bimetallic nanoparticles by supervised machine learning. *Nano Lett.* **2018**, *19*, 520−529.

(63) Ankudinov, A. L.; Ravel, B.; Rehr, J. J.; Conradson, S. D. Real-space multiple-scattering calculation and interpretation of X-ray-absorption near-edge structure. *Phys. Rev. B* **1998**, *58*, 7565−7576.

(64) Ahmadi, M.; Timoshenko, J.; Behafarid, F.; Roldan Cuenya, B. Tuning the structure of Pt nanoparticles through support interactions: an in situ polarized X-ray absorption study coupled with atomistic simulations. *J. Phys. Chem. C* **2019**, *123*, 10666−10676.

(65) Stern, E. EXAFS theory. In *X-ray absorption: principles, applications, techniques of EXAFS, SEXAFS, and XANES*; Koningsberger, D.; Prins, R., Eds. John Wiley and Sons: New York, NY, 1988, 3.

(66) Timoshenko, J.; Duan, Z.; Henkelman, G.; Crooks, R. M.; Frenkel, A. I. Solving the structure and dynamics of metal nanoparticles by combining X-ray absorption fine structure spectroscopy and atomistic structure simulations. *Annu. Rev. Anal. Chem.* **2019**, *12*, 501−522.

(67) Bunker, G. Application of the ratio method of EXAFS analysis to disordered systems. *Nucl. Instrum. Methods Phys. Res.* **1983**, *207*, 437−444.

(68) Glasner, D.; Frenkel, A. I. Geometrical characteristics of regular polyhedra: application to EXAFS studies of nanoclusters. *AIP Conf. Proc.* **2007**, *882*, 746−748.

(69) Sevillano, E.; Meuth, H.; Rehr, J. J. Extended x-ray absorption fine structure Debye-Waller factors. I. Monatomic crystals. *Phys. Rev. B* **1979**, *20*, 4908.

(70) Dalba, G.; Fornasini, P. EXAFS Debye−Waller factor and thermal vibrations of crystals. *J. Synchrotron Radiat.* **1997**, *4*, 243−255.

(71) Timoshenko, J.; Kuzmin, A.; Purans, J. EXAFS study of hydrogen intercalation into ReO_3 using the evolutionary algorithm. *J. Phys.: Condens. Matter* **2014**, *26*, No. 055401.

(72) Gurman, S. J.; McGreevy, R. L. Reverse Monte Carlo simulation for the analysis of EXAFS data. *J. Phys.: Condens. Matter* **1990**, *2*, 9463.

(73) Timoshenko, J.; Kuzmin, A. Wavelet data analysis of EXAFS spectra. *Comput. Phys. Commun.* **2009**, *180*, 920−925.

(74) Stern, E. A.; Ma, Y.; Hanske-Petitpierre, O.; Bouldin, C. E. Radial distribution function in X-ray-absorption fine structure. *Phys. Rev. B* **1992**, *46*, 687−694.

(75) Sutton, A. P.; Chen, J. Long-range Finnis−Sinclair potentials. *Philos. Mag. Lett.* **1990**, *61*, 139−146.

(76) Vila, F. D.; Hayashi, S. T.; Moore, J. M.; Rehr, J. J. Molecular dynamics simulations of supported Pt nanoparticles with a hybrid Sutton−Chen potential. *J. Phys. Chem. C* **2016**, *120*, 14883−14891.

(77) Timoshenko, J.; Keller, K. R.; Frenkel, A. I. Determination of bimetallic architectures in nanometer-scale catalysts by combining molecular dynamics simulations with X-ray absorption spectroscopy. *J. Chem. Phys.* **2017**, *146*, 114201.

(78) Timoshenko, J.; Lu, D.; Lin, Y.; Frenkel, A. I. Supervised machine learning-based determination of three-dimensional structure of metallic nanoparticles. *J. Phys. Chem. Lett.* **2017**, *8*, 5091−5098.

(79) Lytle, F. W.; Greegor, R. B.; Marques, E. C.; Sandstrom, D. R.; Via, G. H.; Sinfelt, J. H. Structural genesis of Pt on SiO_2: determination by X-ray absorption spectroscopy. *J. Catal.* **1985**, *95*, 546−557.

(80) Beni, G.; Platzman, P. M. Temperature and polarization dependence of extended X-ray absorption fine-structure spectra. *Phys. Rev. B* **1976**, *14*, 1514−1518.